https://doi.org/10.1016/j.jallcom.2018.08.192

Control of shear band dynamics in $Cu_{50}Zr_{50}$ metallic glass by introducing amorphous-crystalline interfaces

S.D. Feng [a,b], L. Li [c], K.C. Chan [b,*], L. Qi [a,d], L. Zhao [b], L.M. Wang [a,*], R.P. Liu [a]

[a] *State Key Laboratory of Metastable Materials Science and Technology, Yanshan University, Qinhuangdao 066004, China*

[b] *Advanced Manufacturing Technology Research Centre, Department of Industrial and Systems Engineering, The Hong Kong Polytechnic University, 999077, Hong Kong.*

[c] *Department of Metallurgical and Materials Engineering, The University of Alabama, Tuscaloosa, AL 35487, USA*

[d] *Department of Materials Science and Engineering, The University of Tennessee, Knoxville, Tennessee 37996, USA*

Submitted to

Journal of Alloys and Compounds

As a full paper

* Corresponding author.
E-mail address: kc.chan@polyu.edu.hk; (K.C. Chan),
limin_wang@ysu.edu.cn; (L.M. Wang).

Abstract

The effects of interfaces in crystalline Cu/amorphous $Cu_{50}Zr_{50}$ on shear banding dynamics are investigated using molecular dynamics simulations. The results show that the introduction of amorphous-crystalline interfaces can effectively promote the homogeneous distribution of shear transformation zones (STZs). We found that the high potential energy combined with the defects of the interfaces promote the nucleation of STZs. Further, the amorphous-crystalline interfaces are transition regions that mediate the transmission of dislocations in the crystallites into STZs in the metallic glasses. The accumulation of STZs and dislocations at the interfaces provide the sources for the enhanced plastic deformation in nanocomposites. These results allow us to determine the fundamental atomic structure of amorphous-crystalline interfaces in nanocomposites.

Keywords: *Metallic glass; Shear band; Interface; Molecular dynamics simulation*

1. Introduction

Metallic glasses (MGs) have been attracting attention by virtue of the excellent mechanical and functional properties [1-5]. The major challenge for MGs is in overcoming brittle fractures caused by strain localization [6, 7], and considerable efforts have been made to overcome the low plasticity of MGs [8-16]. The prevailing method to generate more nucleation sites is to introduce a secondary crystalline phase by nucleating or directly introducing second phase particles [17-19]. The advantage is that the introduction of crystallites into the MG matrix can improve the plasticity

without reducing the glass forming ability [20]. Experimental studies have shown that uniform dispersion of crystallites can significantly improve the plasticity of MGs at room temperature [21]. Crystallites, as absorbers for deformation localization, homogenize the nucleation of the STZs and hinder the propagation of shear bands, either by triggering dislocation slippage or phase transformation [22]. The suppressed propagation of the shear bands largely explains the improvement in the plasticity of MGs [23-25]. When adding crystalline phases to MGs, the deformation behavior is modified, and often the weak amorphous-crystalline interfaces are emphasized, showing high energy [26], complex atomic configurations and inconsistencies between structures [27, 28]. This increases resistance to catastrophic crack propagation by forming multiple shear bands. For example, Wang et al. reported that the amorphous–crystal interfaces exhibit unique inelastic shear (slip) transfer characteristics in crystalline copper/copper–zirconium glass nanolaminates, avoiding extreme stress concentrations that lead to fracture initiation, and is considered a pioneering work in the field [29]. The interfaces also affect the crystallization behavior. Simulations have shown that lower interface energies can contribute to smaller critical nucleation sizes and larger activation energies of crystal growth [30]. Another factor is the size of the embedded crystallites, which mainly determines the properties of the MG composites [31]. When the crystallite size is greater than 3 nm, dislocations and twinning could be formed. While the crystallites are small in size, mechanical dissolution occurs and the propagation of shear bands is barely affected [32]. Therefore, it is significant to investigate the effects of the introduced

amorphous-crystalline interfaces on the shear band dynamics, and their dependence on the crystallite size, in order to better understand the deformation of the nanocomposites. Unlike the crystalline-crystalline interfaces that show incompatibility, the amorphous-crystalline interfaces reflect good compatibility features by virtue of the properties of the STZs in MGs [33]. STZs are considered as the basic units of deformation in MGs and can evolve into shear bands upon loading [34-36]. Recently, Zhao et al. found that volume fraction and symmetry of dissimilar STZs can play a very important role in shear banding dynamics and stress-strain behaviors through carrying out STZ dynamics simulations [37, 38]. Proper incorporation of interfaces and crystalline phases can improve the number of the nucleation sites of the shear bands, impeding the growth of mature shear bands [39]. These aspects imply that the plasticity of MGs can be enhanced by introducing amorphous-crystalline interfaces. Although the amorphous-crystalline interfaces could play a key role in the plastic deformation, details of the amorphous-crystalline interfaces are still contentious.

Moreover, studies on the structural change of MGs by virtue of amorphous-crystalline interfaces are largely lacking, and the deformation mechanisms of such nanocomposites remain unclear. It is still challenging to systematically investigate the deformation mechanisms of the nanocomposites through experimental methods considering that the crystalline defects, impurities, interfacial reactions and lattice mismatches all play roles [40]. Therefore, the effects of the introduced amorphous-crystalline interfaces on shear band dynamics are seldomly investigated

experimentally. Molecular dynamics (MD) simulations can allow the study of interfaces at the atomic level, and can be used to supplement experimentation [41-44]. For example, Yamamoto et al. concluded, using MD simulations, that the occurrence of the critical strength in the nanocomposite composed of nanoscale crystallites and MGs is due to the interaction between the dislocation and amorphous phase [45]. Using MD simulations, Shi and Falk found that STZs first take place at the amorphous-crystalline interfaces [46]. Albe et al. identified that glass–glass interfaces can act as structural heterogeneities and prevent strain localization [47]. Zhou et al. concluded that dislocations on the glass–crystal interfaces play a role in the interaction between the crystallites and shear bands through MD simulations [42, 48]. Applying the MD simulations, Brandl et al. investigated the amorphous-crystalline interfaces in Cu/$Cu_{46}Zr_{54}$ multi-layer structures, and found that the production and motion of the interfacial dislocations are closely related to the plastic shear deformation [49]. Through MD simulations, Gao et al. examined the thermal and kinetic properties of amorphous-crystalline interfaces between B2 CuZr and the $Cu_{50}Zr_{50}$ amorphous matrix [50]. Using MD simulations, Adibi et al. found that nanoglasses, composed of nano-scale glassy grains separated by glass-glass interfaces, reveal a transition in the deformation from a single shear band to a uniform superplastic flow when reducing the size of the glassy grain [51-54]. Sha et al. demonstrated that a nanolaminate combining MGs and nano-glass layers of suitable thicknesses can withstand large plastic deformation while maintaining structural stability through MD simulations [55]. To determine a more detailed deformation

mechanism in nanocomposites, we investigated the effects of the introduced amorphous-crystalline interfaces on the shear band dynamics and their dependence on the crystallite size in Cu/$Cu_{50}Zr_{50}$ (labelled as Cu/CuZr) nanocomposites using MD simulations. We focused on the atomic structure of the amorphous-crystalline interfaces and their effects on the nucleation and propagation of the shear bands.

2. Methods

Based on the embedded atom method (EAM) potential developed by Mendelev et al., MD simulations were performed in LAMMPS [56]. In this work, the Cu-Zr system was selected because of its reliable empirical potential and excellent glass-forming ability. The random $Cu_{50}Zr_{50}$ configuration, of dimensions around 4.6×4.6×4.6 nm^3, was composed of 2500 Cu atoms and 2500 Zr atoms. It was equilibrated at 2000 K and zero pressure for 1 ns to ensure chemical homogeneity. The model was quenched to 50 K at a cooling rate of 10^{10} K/s under periodic boundary conditions (PBCs) using a Nose-Hoover thermostat within a NPT ensemble (constant number, constant pressure, and constant temperature) [57, 58]. A Parrinello-Rahman technique was adopted to maintain the zero-pressure [59]. The quenching rate was chosen to facilitate strain localization and to avoid the growth of crystallites under deformation. The big MG models, containing 250,000 atoms (21.5×4.3×43 nm^3) were then prepared by replicating the small $Cu_{50}Zr_{50}$ MG. To investigate the effects of the introduced amorphous-crystalline interfaces on the shear band dynamics and their dependence on crystallite size, we introduced different sized crystallite Cu oriented in the [111] direction aligned with the z-direction. The selected

orientation makes the direction of maximum shear stress appear on the slip plane so that dislocations can be directed to the interface [60]. The sizes of different crystallite Cu are listed in Table 1, but the volume fractions of crystallite Cu are all 20%. Subsequently, matching rectangular blocks were cut from the MG models to fill the crystallite Cu. The nanocomposites were prepared by combining the MG with crystalline Cu. In order to obtain a more relaxed/realistic interface between the crystallites and MGs, the models were relaxed at 1.5 GPa and 50 K for 1 ns, during which the atoms in the crystallites were fixed. Then, the models were relaxed at 0 GPa and 50 K for 1 ns to release the excess energy.

The nanocomposites were simulated at the temperature of 50 K by moving the rigid atoms at one end along the *Z*-direction, while keeping the rigid atoms at the other end unchanged. The command of "displace_atoms" in the LAMMPS code was used to perform the compression of the samples when the Z-direction was kept free surface. We adopted the inhomogeneous compression deformation, namely applying an instantaneous and small strain to the system, and then relaxing it. The deformation cycle is then repeated. In each cycle, the moving end was moved 0.017 nm in an instant, then the whole sample experienced relaxation for 10 ps. Since each timestep is about 10^{-15} second, the typical strain rate used in this work is about 4×10^{7} s^{-1}. Note that a Parrinello-Rahman barostat was employed in the *Y*-direction perpendicular to the loading *Z*-direction to achieve stress-free state. The low temperature of 50 K is chosen to generate failure by shear banding [51, 61]. A PBC was enforced along the *Y*-direction while both *X*- and *Z*-directions were kept free surfaces. The existence of

free surfaces is a key factor that contributes to form shear bands [62]. To visulize the interfaces, common neighbor analysis (CNA) was conducted to characterize and color-code the local structural environment of an atom. By comparing the current atomic configuration with the initial configuration, the von Mises strain η^{Mises} could be utilized to quantify the shear deformation in MGs, which was originally proposed by Shimizu et al. [63]. The large η^{Mises} shows that the atoms experience large local shear strain [51, 64]. The CNA and η^{Mises} were implemented in the open visualization tool (OVITO) [65], allowing a direct observation of the various deformation modes with atomic resolution.

Table 1. The sizes of different crystallite Cu

Label	S1	S2	S3
Size ($Å^3$)	30 Å × 43 Å × 60 Å	43 Å × 43 Å × 60 Å	72 Å × 43 Å × 60 Å

3. Results

3.1. Overall mechanical response of the nanocomposites

By comparing the stress-strain curves, the differences in the overall mechanical response of materials can be reflected. The compressive stress–strain curves of the nanocomposites with three different crystallite sizes and the monolithic MG are displayed in Fig. 1(a). For convenience, the four models are labeled as S1, S2, S3 and as cast, respectively. As shown in Fig. 1(a), the mechanical responses of the nanocomposites are seriously influenced by the crystallite size. In all the nanocomposites, the compressive stress increases to the peak stress τ_y, which corresponds to nucleation of the shear bands. For the S1 nanocomposite, the dropping

stress is gradual after the maximum stress, while for the S2 and S3 nanocomposites, with larger crystalline Cu, the models experience a sudden drop in stress, which corresponds to deformation localization into shear bands [61]. The situation is the same as that of the monolithic MG. After yielding, the stress–strain curves show balanced patterns, corresponding to the flow stress τ_s. As shown in Fig. 1(b), the maximum stress and flow stress increase with increasing crystallite size. For example, τ_y and τ_s are the highest for model S3. Recent simulation studies and theoretical models showed that the value of ($\Delta\tau=\tau_y-\tau_s$) in Fig. 1(b) corresponds to a change in plastic response because of the structural softening determined by the tendency toward strain localization [62, 66, 67]. The smaller the $\Delta\tau$, the better the plasticity. The stress drop ($\Delta\tau=\tau_y-\tau_s$) values calculated in our simulations are 0.34 GPa, 0.56 GPa, 0.63 GPa and 0.78 GPa for the S1, S2, S3 nanocomposites and as cast, respectively. Compared to the monolithic MG, the stress drop ($\Delta\tau=\tau_y-\tau_s$) is significantly reduced for nanocomposites at the yield point, and the smaller the crystallites, the smaller the $\Delta\tau$. The stress drop ($\Delta\tau=\tau_y-\tau_s$) values of the S1 nanocomposite is reduced by 54% compared to the monolithic MG, showing enhanced plastic flow behavior. From the above results, it is noted that the introduction of the amorphous-crystalline interfaces can significantly change the yield stress and flow stress, and is consistent with the works of Wang et al. and Yamamoto et al. [29].

These models exhibit different elastic moduli and ductility. Young's modulus is calculated based on the rule of mixtures. This is the iso-strain condition for the upper

bound:

$$E_m = f_c E_{c+} f_a E_a \quad (1)$$

The iso-stress sets the lower bound:

$$1/E_m = f_c/E_{c+} f_a/E_a \quad (2)$$

where f_c and f_a are the corresponding volume fractions of crystallites and MGs. E_c and E_a are Young's moduli of the crystallites and MGs. Young's modulus of MG $Cu_{50}Zr_{50}$ is 55 GPa, and that of crystalline Cu is 109 GPa, respectively. The volume fractions of the crystallites in the three nanocomposites are all 20%, so Young's modulus calculated by the rule of mixtures in the iso-strain condition is 65.8 GPa, while that in the iso-stress condition is 61.4 GPa. Young's modulus values calculated by our simulations are 45.5 GPa, 57.1 GPa and 64.5 GPa for the S1, S2 and S3 nanocomposites, respectively. In comparision with the value predited by the rule of mixtures, the simulated Young's modulus values of the S1 and S2 nanocomposites are smaller than that of the lower bound (61.4 GPa). The drop in elastic modulus is large for the S1 nanocomposite with smallest crystallites. Young's modulus of the S3 nanocomposite is between the upper and lower bound calculated by the rule of mixtures due to the relatively small number of interfaces in the S3 nanocomposite. The larger values based on the rule of mixtures are due to strain compatibility and displacement continuity [68]. The rule of mixtures assumes that nano-composites are made of hard crystallites and a soft amorphous matrix. If the two-phase assumption is true, the modulus of the composite should fall in the range between the iso-strain and iso-stress values. However, the simulated S1 and S2 samples exhibit moduli even

lower than the lower bound set by the iso-stress condition, attesting to the fact that the two-phase assumption does not hold. In other words, there has to be another 'phase' with an even lower modulus than that of the amorphous phase, that is the amorphous-crystalline interface. Indeed, our detailed analysis shows that the amorphous-crystalline interface is a weaker interface, exhibiting higher disorder and energy. The effects of the amorphous-crystalline interfaces on different stages of the shear banding process are discussed in the following sections.

3.2. The interface effect on the shear band initiation

As seen in Fig. 1(a), the S1 nanocomposite shows enhanced plastic flow behavior. So, the S1 nanocomposite is selected to investigate the interface effect on the shear band initiation. For the S1 model, the atomic local shear strain at macroscopic strains of 3%, 5% and 10% are respectively shown in Fig. 2(a)–(c). As shown in Fig. 2(a), plastic deformation is initiated at the amorphous-crystalline interfaces which then becomes the shear band nuclei in the MG. Further straining, from the nuclei, induces multiple incipient shear bands to form, as shown in Fig. 2(b). They intersect and overlap, expanding over a broad region in the MG. As the load increases, as shown in Fig. 2(c), the interactions of the shear bands in the MG undertake large strain. The incorporation of crystallites in the nanocomposites results in the formation of amorphous-crystalline interfaces. The unique amorphous-crystalline interfaces, that are quantified in the following, serve as the nucleation sites for the multiple shear bands, effectively distributing the plastic flow and leading to nearly perfect plastic behavior in the stress-strain curve of the

nanocomposite S1, as shown in Fig. 1(a).

To elucidate the underlying deformation mechanisms that occur first at the amorphous-crystalline interfaces, the potential energy and defects at the interfaces were calculated at the initial configuration prior to deformation in the S2 nanocomposite. As shown in Fig. 3(a), only atoms with potential energy larger than -3 eV/atom are displayed. Although the energy of the amorphous-crystalline interfaces is lower than that of crystalline-crystalline interfaces, the atomic potential energy at the amorphous-crystalline interfaces is higher than that of MGs and crystallites. The Voronoi tessellation method can identify the neighbors of each atom in MGs. Each face of the Voronoi polyhedron corresponds to one of the neighbors of the central atom. When two faces of a Voronoi polyhedron share an edge, the two corresponding atoms of the two faces are called a pair of adjacent atoms. If the pair of adjacent atoms is not the nearest neighbors of each other, the pair of adjacent atoms are called as a pair of quasi-nearest atoms (QNAs) [69]. Therefore, QNAs can represent the regions of configurational disorder. As shown in Fig. 3(b), only atoms with the number of QNA (N_Q) larger than 5 atoms are shown, which suggests that the defects in the interfaces are more than that in the MGs and the crystallites.

We calculated the atomic Voronoi volumes for all atoms in the undeformed S2 nanocomposites and averaged them in the direction perpendicular to the loading direction. This is very effective in determining the interface region based on the atomic Voronoi volume [52, 70]. As shown in the dotted rectangle of Fig. 3(c), the amorphous-crystalline interface region perpendicular to the x-axis is defined.

Similarly, the interface region parallel to the x-axis is also defined. The average Voronoi volumes of the amorphous-crystalline interfaces, MGs and crystallites are 14.9 $Å^3$, 13.48 $Å^3$ and 12.08 $Å^3$, respectively. It shows that the average free volume of the amorphous-crystalline interface is larger, or in other words the density is smaller, than that of the MG and crystallite. Through the spatial distributions of Voronoi volumes, we progressively distinguished the interface region. Because of the defects in the interfaces, a slightly increased atomic volume of the interfaces accompanies deformation, indicating that an increased volume will lead to a more homogeneous distribution of STZs, resulting in deformation at various positions. So the interfaces of crystallites and MGs, as the weaker regions, will promote the accommodation of stress and the initiation of shear bands.

3.3. The interface effect on the coupling of dislocation and shear band

Amorphous-crystalline interfaces are the nucleation locations for the shear bands. However, these shear bands cannot propagate freely because they are blocked by the crystallites. As the load increases, the crystallites also take part in the deformation to release the stress of the nanocomposites. Fig. 4(a) shows the atomic displacement (yellow arrows) and local shear strain (atomic color) diagram of the part S1 nanocomposite at the strain of 4%. Compared with atoms outside the interfaces, the atoms at the interfaces move desultorily since the atomic potential energy at the amorphous-crystalline interfaces is higher than that of MGs and crystallites, which activates atoms in MGs. The role of the interfaces is similar to that of the grain boundaries in crystalline materials. Desultory movement of atoms at the interfaces

promotes the formation of STZs and multiple shear bands in the MGs. Shear bands often form at free surfaces before the yield stress is reached. However, owing to the stress concentration and high potential energy at the amorphous-crystalline interfaces, the shear bands nucleate at these interfaces, indicating that the nucleation barriers at the interfaces are lower than those at the surfaces. The evolution of shear bands in the interfaces in our model is consistent with that observed in other experiments [71, 72]. They found that the interface between the glass matrix and quasicrystals could act as a source for the multiple shear band initiation, achieving plastic strains larger than 6% at room temperature.

Fig. 4(b) shows the Common Neighborhood Parameter (CNP) of the portion of the S1 nanocomposite at the strain of 4%. The CNP proposed by Tsuzuki et al. can effectively characterize the local lattice order around one atom [73]. With this parameter, we can determine whether an atom is part of a perfect lattice, a local defect (including dislocations and stacking faults), or at a surface. A parameter Q_i is used to evaluate the CNP for each atom i, as follows:

$$Q_i = \frac{1}{n_i}\sum_{j=1}^{n_i} \left| \sum_{k=1}^{n_{ij}} (\boldsymbol{R}_{ij} + \boldsymbol{R}_{jk}) \right|^2 \quad (3)$$

where the index j goes over the n_i nearest neighbors of atom i, and the index k goes over the n_{ij} common nearest neighbors between atom i and atom j. $\mathbf{R}_{ik}$ is the vector connecting atom i to atom k. For example, in perfect fcc and bcc structures, the Q_i is 0; in a hcp structure, the Q_i is 4.4 Å^2; in a fcc (111) surface, the Q_i is 13 Å^2. The average CNP values of the amorphous-crystalline interfaces, MGs and crystallites were 21.6 Å^2, 24.3 Å^2 and 0 Å^2, respectively. As shown in Fig. 4(b), the CNP value of the

amorphous-crystalline interfaces (white rectangle) is smaller than that of the MG but larger than that of the crystalline Cu. Therefore, amorphous-crystalline interfaces are transition regions from crystallites to MGs, allowing transmission of the dislocation-mediated slip into shear bands. Through coupling atom probe tomography and transmission electron microscopy, Guo et al. found that crystallographic slip bands in the crystalline Cu coincide with shear bands in the CuZr MGs, and dislocations from the crystalline Cu can drag Cu atoms across the interface into the CuZr MGs. [74], showing that our results are in alignment with their findings. As shown in Fig. 5(a), the stacking faults formed via atomic shuffling at the interfaces are accompanied by the 1/6 <112> Shockley partial dislocation nucleation. With the further loading shown in Fig. 5(b), the leading partial dislocations move across the whole crystallites and hit the opposite interfaces, leading to the expansion of the stacking faults across the crystalline Cu. In Fig. 5(c), more stacking faults are activated near the amorphous-crystalline interfaces. Cheng and Trelewicz found that when dislocations slide at the amorphous-crystalline interfaces, they can be absorbed into the MG, which in turn triggers the activation of new STZs [75].

To further investigate the coupling of the dislocations and shear bands, the atomic structure of the crystallites at strains of 0% and 10% is shown in Fig. 6. By comparing the atomic structure of the crystallites at strains of 0% and 10%, it is found that some of the crystallite involve dissolution processes, as denoted in the red ovals in Fig. 6, and some of the crystallite transforms from FCC (green) to stack fault (red), which undertakes the deformation. At the strain of 10%, the ratios of the stack

fault/FCC were 13.87%, 5.79% and 3.3% for crystallites in the S1, S2 and S3 nanocomposites, respectively, which suggests that the number of stacking faults increases with the decrease of crystallite size. Consequently, increasing number of stacking faults promotes dislocation and shear band coupling.

3.4. The interface effect on the shear band propagation

To understand the deformation of nanocomposites, the images of the local atomic shear strain of Cu/CuZr nanocomposites with different crystalline sizes at the strain of 10% are shown in Fig. 7, where all atoms are colored according to η_{Mises}. Compared to the monolithic MG, the crystallites in the nanocomposites can impede the propagation of shear bands, causing the shear bands to bend and branch. Adibi et al. also found that when the shear bands generated in the MG layer propagate and reach the nanoglass-MG interfaces, they do not further cause local plastic deformation in the nanoglass layer [54]. Our results are consistent with their findings. The ability of the crystallites to prevent the shear bands from expanding is greatly influenced by the crystallite size. A transition from shear band domination to plastic co-deformation can be identified as the crystallite size decreases. As shown in Fig. 7(b)-(d), two main shear bands form in a crisscross manner throughout the S2 nanocomposite, the S3 nanocomposite and the monolithic MG. The crystallites cannot block the propagation of the shear bands in Fig. 7(b) and 7(c). In the stress-strain curves, the stress drops are all abrupt after yielding in the S2 nanocomposite, the S3 nanocomposite and the monolithic MG. Therefore, the deformation of nanocomposites is dominated by the shear bands among them. For the S1 nanocomposite, plastic co-deformation of the

shear bands and dislocations is achieved. With the stress drop not being abrupt but gradual in stress-strain curves, the homogenous distributions of the STZs correspond to the interaction of the multiple shear bands, as shown in Fig. 7(a), and dislocations in the crystallites can strengthen the interactions of shear bands. Although the crystalline fractions in the three composites are the same, the small crystallites in the S1 nanocomposite can effectively hinder the shear band propagation. The main reason is that the small crystallites induce a larger volume of the amorphous-crystalline interfaces, as demonstrated in the above result. We could predict the yielding may transit from the Mohr–Coulomb type to the von Mises type as the particle size of the crystalline phase decreases in the nanocomposites, in particular when the dislocation activities become the primary source of plasticity.

As shown in Fig. 8, the proportions of atoms with η^{Mises} greater than the threshold value of 0.2 for the nanocomposites are calculated in order to remove the effects of the structural and thermal fluctuations [64]. The localization and failure of the models can be estimated. In Fig. 8, S2 and S3 models have almost the same proportions before the strain of 5%. For the S1 nanocomposite, the increase of the proportion after the strain of 4% is nearly linear, which is in good agreement with the stable plastic flow shown in Fig. 1(a). For the as cast MG, the fraction suddenly increases at the strain of 5%, corresponding to the mature shear bands. Meanwhile, the fraction of as cast case is lower than those for the nanocomposites at the strain of 10%, which explains that the flow stresses of the nanocomposites are all higher than that of the monolithic MG. From the above results, the small crystallites result in a sizeable

percentage of the interfaces blocking the shear band propagation, which promotes uniform plastic deformation.

4. Discussion

4.1 The interface effect on the yield stress

As shown in Fig. 1b, the yield stress of the monolithic MG is smaller than that of the S2 and S3 nanocomposites but larger than that of the S1 nanocomposite. The average Voronoi volumes of the amorphous-crystalline interfaces, MGs and crystallites were 14.9 $Å^3$, 13.48 $Å^3$ and 12.08 $Å^3$, respectively. Because of the defects in the interfaces, a slightly increased atomic volume of the interfaces accompanies higher disorder of the atomic structure. Therefore, the strength of interfaces is weaker than that of MGs and crystallites. An interesting question arises as to why the S2 and S3 nanocomposites with weaker interfaces have a higher yield strength compared to the as-cast MG. The images of the local atomic shear strain of the nanocomposites and the monolithic MG at the strain of 4% (the yield point) are shown in Fig. 9. Smaller crystallites can promote the formation of more amorphous-crystalline interfaces, increasing the number of nucleation sites of STZs, as shown in Fig. 9(a). In comparison to the monolithic MG, the reduction in the yield stress of the S1 nanocomposite can be attributed to the existence of lots of amorphous-crystalline interfaces, and the interfaces are anticipated to be even weaker than the MGs. Although there are amorphous-crystalline interfaces in S2 and S3 nanocomposites, triggered deformation of crystallites is more difficult than that of MGs due to dislocation enhancement, which increases the yield strength. The large crystallites

induce a smaller volume of the amorphous-crystalline interfaces, making dislocation enhancement dominate. For example, at the strain of 4%, in Fig. 1(a), before yielding, hardening can be seen in the S2 and S3 nanocomposites. And in Fig. 9(b) and Fig. 9(c), the extent of the atoms participating in STZs (red color) is obviously less than that in the S1 nanocomposite. However, the total strain of these nanocomposites are all 4%. This suggests that some atoms of the S2 and S3 nanocomposites participate in dislocation movements. The dislocation enhancement plays a dominant role in the S2 and S3 nanocomposites, while the amorphous-crystalline interface plays a dominant role in the S1 nanocomposite. This is because the high fraction, atomic structure and degree of disorder of the interfaces lead to a transition from phase-dominant yielding to interface-dominant yielding. This also explains why the drop in elastic modulus is large for the S1 nanocomposite with the smallest crystallites, as shown in Fig. 1(a).

To further investigate the transition mechanism, potential energy of the initial configuration prior to deformation in the S1, S2 and S3 nanocomposites were calculated. For the convenience of observation, only atoms with potential energy greater than -3 eV/atom are displayed in Fig. 10. The density of atoms with potential energy greater than -3 eV/atom at the interfaces in the S1 nanocomposite is larger than that in the S2 and S3 nanocomposites. Because the atoms with larger potential energy are more prone to move, interface-dominant yielding occurs in the S1 nanocomposite. While atoms with the potential energy greater than -3 eV/atom at the interfaces in the S2 and S3 nanocomposites are relatively few, this cannot stimulate the generation of more nucleation sites for STZs. Therefore, dislocation movements in

crystallites are activated, bearing a part of the deformation.

4.2 The interface effect on the flow stress

The small crystallites effectively block the shear bands since triggered deformation of crystallites is more difficult to achieve than for MGs, which increases the flow stress. The dislocation motion is pinned and stopped at the opposite interfaces in this work. Therefore, the flow stresses of the S2 and S3 nanocomposites are obviously higher than that of the as-cast MG, which can be attributed to the activity of the dislocations in the crystalline region. Hufnagel et al found that the dislocations in crystallites could strengthen the interactions of shear bands [32], which is consistent with our results in Fig. 1(a). However, for the S1 nanocomposite, the increase in the interface fractions leads to a transition from phase-dominant yielding to interface-dominant yielding, which decreases the flow stress, resulting in a slightly higher flow stress in the S1 sample compared to that of the monolithic MG.

4.3 The interface effect on the coupled deformation processes

As shown in Fig. 11, the desultory movement of atoms in the interfaces promote STZs near the interfaces in MGs, and dislocations or stacking faults in crystallites. Dislocations and stacking faults dominate the deformation of the crystalline Cu, while STZs or shear bands play a dominant role in the plastic deformation of the MG. The high nucleation stress promotes the nucleation of dislocations in crystalline Cu. Once dislocations cross the interface, they will be absorbed, which means that the dislocations at the interface will be stress concentration points, thereby facilitating the formation of more STZs near the interface. The accumulation of STZs and

dislocations at the interfaces provide the sources for enhanced plastic deformation in nanocomposites.

4.4 Limitation

The size and time scale in MD simulations deviate massively from that in experiments by virtue of current computer power limitations. Therefore, the boundary of the crystallites in our models is rectangle not spherical. If the size of the spherical crystallites is too small, it is easy to dissolve these crystallites during deformation due to their high surface tension. However, it must be remembered that the deformation behavior of nanocomposites can be influenced by the shape of crystallites. In fact, this is a huge challenge in the field of computational simulations. Nevertheless, the role of interfaces investigated by MD simulations can aid in understanding nanocomposites during deformation. In future work, the effect of free surfaces and crystallite shapes will be investigated.

5. Conclusions

Control of the shear band dynamics in the $Cu_{50}Zr_{50}$ MG by introducing amorphous-crystalline interfaces was investigated by MD simulations. The introduction of the amorphous-crystalline interfaces can significantly change the yield stress and flow stress. The stress drop ($\Delta\tau=\tau_y-\tau_s$) values of the nanocomposite with smallest crystallites is reduced by 54% compared to the monolithic MG. The small crystallites in the S1 nanocomposite, resulting in a sizeable interfaces percentage, improve the deformation ability. The atomic potential energy and defects characterized by the QNA of the interfaces are higher than those of MGs and

crystallites. The desultory movement of atoms in the interfaces promote the formation of STZs near the interfaces in MGs. The CNP value of the amorphous-crystalline interfaces is smaller than that of the MG but larger than that of crystalline Cu, which makes the amorphous-crystalline interfaces the transition regions from crystallites to MGs, mediating the transmission of dislocation slips into shear bands. Stacking faults form via atomic shuffling across the crystalline Cu, followed by 1/6 <112> Shockley partial dislocations, which can be stress concentration points near the interfaces. The accumulation of STZs and dislocations at the interfaces provide the sources for enhanced plastic deformation in nanocomposites. The results obtained not only provide a better understanding of the deformation mechanism of nanocomposites, but also serve as a guide to the design of new MG composites with excellent mechanical properties.

Acknowledgments

This work was supported by the Hong Kong Scholars Program (Grant No. XJ2017049), the Hong Kong Polytechnic University (Grant No. G-YZ1J) and the Program for the Top Young Talents of Higher Learning Institutions of Hebei (Grant No. BJ2018021). LL would like to acknowledge the support from the National Science Foundation under grant number CMMI 17-0267.

References

[1] J.C. Qiao, Y. Yao, J.M. Pelletier, L.M. Keer, Understanding of micro-alloying on plasticity in $Cu_{46}Zr_{47-x}Al_7Dy_x$ ($0 \leq x \leq 8$) bulk metallic glasses under compression: Based on mechanical relaxations and theoretical analysis, Int. J. Plast., 82 (2016) 62-75.

[2] H.B. Lu, L.C. Zhang, A. Gebert, L. Schultz, Pitting corrosion of Cu-Zr metallic glasses in hydrochloric acid solutions, J. Alloys Compd., 462 (2008) 60-67.

[3] A. Gebert, P. Gostin, M. Uhlemann, J. Eckert, L. Schultz, Interactions between mechanically generated defects and corrosion phenomena of Zr-based bulk metallic glasses, Acta Mater., 60 (2012) 2300-2309.

[4] D.Z. Chen, C.Y. Shi, Q. An, Q. Zeng, W.L. Mao, W.A. Goddard, J.R. Greer, Fractal atomic-level percolation in metallic glasses, Science, 349 (2015) 1306-1310.

[5] J.R. Greer, J.T.M. De Hosson, Plasticity in small-sized metallic systems: Intrinsic versus extrinsic size effect, Prog. Mater. Sci., 56 (2011) 654-724.

[6] A. Greer, Y. Cheng, E. Ma, Shear bands in metallic glasses, Mater. Sci. Eng., R, 74 (2013) 71-132.

[7] W. Chen, H. Zhou, Z. Liu, J. Ketkaew, N. Li, J. Yurko, N. Hutchinson, H. Gao, J. Schroers, Processing effects on fracture toughness of metallic glasses, Scripta Mater., 130 (2017) 152-156.

[8] H.F. Zhou, C. Zhong, Q.P. Cao, S.X. Qu, X.D. Wang, W. Yang, J.Z. Jiang, Non-localized deformation in metallic alloys with amorphous structure, Acta Mater., 68 (2014) 32-41.

[9] D. Şopu, C. Soyarslan, B. Sarac, S. Bargmann, M. Stoica, J. Eckert, Structure-property relationships in nanoporous metallic glasses, Acta Mater., 106 (2016) 199-207.

[10] G. He, J. Eckert, W. Loser, L. Schultz, Novel Ti-base nanostructure-dendrite composite with enhanced plasticity, Nat. Mater., 2 (2003) 33-37.

[11] Z.F. Zhang, G. He, J. Eckert, L. Schultz, Fracture mechanisms in bulk metallic glassy materials, Phys. Rev. Lett., 91 (2003) 045505.

[12] J.C. Qiao, J.M. Pelletier, Analysis of atomic mobility in a $Cu_{38}Zr_{46}Ag_8Al_8$ bulk metallic glass, J. Alloys Compd., 549 (2013) 370-374.

[13] J.C. Qiao, J.M. Pelletier, C. Esnouf, Y. Liu, H. Kato, Impact of the structural state on the mechanical properties in a Zr-Co-Al bulk metallic glass, J. Alloys Compd., 607 (2014) 139-149.

[14] J.C. Qiao, J.M. Pelletier, Influence of thermal treatments and plastic deformation on the atomic mobility in $Zr_{50.7}Cu_{28}Ni_9Al_{12.3}$ bulk metallic glass, J. Alloys

Compd., 615 (2014) S85-S89.

[15] D.Z. Chen, X.W. Gu, Q. An, W.A. Goddard, J.R. Greer, Ductility and work hardening in nano-sized metallic glasses, Appl. Phys. Lett., 106 (2015) 061903.

[16] D.Z. Chen, D. Jang, K.M. Guan, Q. An, W.A. Goddard, 3rd, J.R. Greer, Nanometallic glasses: size reduction brings ductility, surface state drives its extent, Nano Lett., 13 (2013) 4462-4468.

[17] K. Song, S. Pauly, Y. Zhang, R. Li, S. Gorantla, N. Narayanan, U. Kühn, T. Gemming, J. Eckert, Triple yielding and deformation mechanisms in metastable $Cu_{47.5}Zr_{47.5}Al_5$ composites, Acta Mater., 60 (2012) 6000-6012.

[18] S. Pauly, G. Liu, G. Wang, U. Kühn, N. Mattern, J. Eckert, Microstructural heterogeneities governing the deformation of $Cu_{47.5}Zr_{47.5}Al_5$ bulk metallic glass composites, Acta Mater., 57 (2009) 5445-5453.

[19] J.C. Li, X.W. Chen, F.L. Huang, On the mechanical properties of particle reinforced metallic glass matrix composites, J. Alloys Compd., 737 (2018) 271-294.

[20] X. Tong, G. Wang, J. Yi, J. Ren, S. Pauly, Y. Gao, Q. Zhai, N. Mattern, K. Dahmen, P. Liaw, Shear avalanches in plastic deformation of a metallic glass composite, Int. J. Plast., 77 (2016) 141-155.

[21] S. Pauly, S. Gorantla, G. Wang, U. Kuhn, J. Eckert, Transformation-mediated ductility in CuZr-based bulk metallic glasses, Nat. Mater., 9 (2010) 473-477.

[22] C. Sterwerf, T. Kaub, C. Deng, G.B. Thompson, L. Li, Deformation mode transitions in amorphous-$Cu_{45}Zr_{55}$/crystalline-Cu multilayers, Thin Solid Films, 626 (2017) 184-189.

[23] M.H. Yang, J.H. Li, B.X. Liu, Local structure evolutions of metallic glasses during shear deformation investigated by computer simulations, J. Alloys Compd., 735 (2018) 1023-1030.

[24] H.Y. Zhang, G.P. Zheng, Simulation of shear banding in bulk metallic glass composites containing dendrite phases, J. Alloys Compd., 586 (2014) S262-S266.

[25] G.J. Yang, B. Xu, L.T. Kong, J.F. Li, S. Zhao, Size effects in $Cu_{50}Zr_{50}$ metallic

glass films revealed by molecular dynamics simulations, J. Alloys Compd., 688 (2016) 88-95.

[26] V. Kokotin, H. Hermann, J. Eckert, Theoretical approach to local and effective properties of BMG based matrix-inclusion nanocomposites, Intermetallics, 30 (2012) 40-47.

[27] L. Huang, J. Zhou, S. Zhang, Y. Wang, Y. Liu, Effects of interface and microstructure on the mechanical behaviors of crystalline Cu-amorphous Cu/Zr nanolaminates, Mater. Des., 36 (2012) 6-12.

[28] P.Y. Zhao, Y.Z. Wang, S.R. Niezgoda, Microstructural and micromechanical evolution during dynamic recrystallization, Int. J. Plast., 100 (2018) 52-68.

[29] Y. Wang, J. Li, A.V. Hamza, T.W. Barbee, Jr., Ductile crystalline-amorphous nanolaminates, Proc. Natl. Acad. Sci. USA, 104 (2007) 11155-11160.

[30] X.Z. Gao, M.H. Müser, L.T. Kong, J.F. Li, Atomic structure and energetics of amorphous–crystalline CuZr interfaces: a molecular dynamics study, Modell. Simul. Mater. Sci. Eng., 22 (2014) 065007.

[31] Y. Wu, H. Wang, H.H. Wu, Z.Y. Zhang, X.D. Hui, G.L. Chen, D. Ma, X.L. Wang, Z.P. Lu, Formation of Cu-Zr-Al bulk metallic glass composites with improved tensile properties, Acta Mater., 59 (2011) 2928-2936.

[32] T.C. Hufnagel, C.A. Schuh, M.L. Falk, Deformation of metallic glasses: Recent developments in theory, simulations, and experiments, Acta Mater., 109 (2016) 375-393.

[33] E.R. Homer, D. Rodney, C.A. Schuh, Kinetic Monte Carlo study of activated states and correlated shear-transformation-zone activity during the deformation of an amorphous metal, Phys. Rev. B, 81 (2010) 064204.

[34] L. Li, E.R. Homer, C.A. Schuh, Shear transformation zone dynamics model for metallic glasses incorporating free volume as a state variable, Acta Mater., 61 (2013) 3347-3359.

[35] D. Sopu, A. Stukowski, M. Stoica, S. Scudino, Atomic-level processes of shear band nucleation in metallic glasses, Phys. Rev. Lett., 119 (2017) 195503.

[36] J.C. Qiao, Y.J. Wang, J.M. Pelletier, L.M. Keer, M.E. Fine, Y. Yao,

Characteristics of stress relaxation kinetics of $La_{60}Ni_{15}Al_{25}$ bulk metallic glass, Acta Mater., 98 (2015) 43-50.

[37] P.Y. Zhao, J. Li, J.W. Hwang, Y.Z. Wang, Influence of nanoscale structural heterogeneity on shear banding in metallic glasses, Acta Mater., 134 (2017) 104-115.

[38] P.Y. Zhao, J. Li, Y.Z. Wang, Heterogeneously randomized STZ model of metallic glasses: Softening and extreme value statistics during deformation, Int. J. Plast., 40 (2013) 1-22.

[39] B.A. Sun, K.K. Song, S. Pauly, P. Gargarella, J. Yi, G. Wang, C.T. Liu, J. Eckert, Y. Yang, Transformation-mediated plasticity in CuZr based metallic glass composites: A quantitative mechanistic understanding, Int. J. Plast., 85 (2016) 34-51.

[40] C.R. Dandekar, Y.C. Shin, Molecular dynamics based cohesive zone law for describing Al–SiC interface mechanics, Composites Part A, 42 (2011) 355-363.

[41] E. Alishahi, C. Deng, Orientation dependent plasticity of metallic amorphous-crystalline interface, Comput. Mater. Sci., 141 (2018) 375-387.

[42] H.F. Zhou, S.X. Qu, W. Yang, An atomistic investigation of structural evolution in metallic glass matrix composites, Int. J. Plast., 44 (2013) 147-160.

[43] Y. Ritter, D. Şopu, H. Gleiter, K. Albe, Structure, stability and mechanical properties of internal interfaces in $Cu_{64}Zr_{36}$ nanoglasses studied by MD simulations, Acta Mater., 59 (2011) 6588-6593.

[44] C.X. Peng, D. Şopu, K.K. Song, Z.T. Zhang, L. Wang, J. Eckert, Bond length deviation in CuZr metallic glasses, Phys. Rev. B, 96 (2017) 174112.

[45] S. Yamamoto, Y.-J. Wang, A. Ishii, S. Ogata, Atomistic Design of High Strength Crystalline-Amorphous Nanocomposites, Mater. Trans., 54 (2013) 1592-1596.

[46] Y. Shi, M.L. Falk, A computational analysis of the deformation mechanisms of a nanocrystal–metallic glass composite, Acta Mater., 56 (2008) 995-1000.

[47] K. Albe, Y. Ritter, D. Şopu, Enhancing the plasticity of metallic glasses: Shear band formation, nanocomposites and nanoglasses investigated by molecular dynamics simulations, Mech. Mater., 67 (2013) 94-103.

[48] H.F. Zhou, H.J. Gao, A plastic deformation mechanism by necklace dislocations near crack-like defects in nanotwinned metals, J. Appl. Mech., 82 (2015) 071015.

[49] C. Brandl, T.C. Germann, A. Misra, Structure and shear deformation of metallic crystalline-amorphous interfaces, Acta Mater., 61 (2013) 3600-3611.

[50] X.Z. Gao, G.Q. Yang, B. Xu, C. Qi, L.T. Kong, J.F. Li, Atomic structure and thermal stability of interfaces between metallic glass and embedding nano-crystallites revealed by molecular dynamics simulations, J. Alloys Compd., 647 (2015) 331-337.

[51] S. Adibi, Z.D. Sha, P.S. Branicio, S.P. Joshi, Z.S. Liu, Y.W. Zhang, A transition from localized shear banding to homogeneous superplastic flow in nanoglass, Appl. Phys. Lett., 103 (2013) 211905.

[52] S. Adibi, P.S. Branicio, Y.W. Zhang, S.P. Joshi, Composition and grain size effects on the structural and mechanical properties of CuZr nanoglasses, J. Appl. Phys., 116 (2014) 043522.

[53] S. Adibi, P.S. Branicio, S.P. Joshi, Suppression of shear banding and transition to necking and homogeneous flow in nanoglass nanopillars, Sci. Rep., 5 (2015) 15611.

[54] S. Adibi, P.S. Branicio, R. Ballarini, Compromising high strength and ductility in nanoglass–metallic glass nanolaminates, RSC Adv., 6 (2016) 13548-13553.

[55] Z.D. Sha, P.S. Branicio, H.P. Lee, T.E. Tay, Strong and ductile nanolaminate composites combining metallic glasses and nanoglasses, Int. J. Plast., 90 (2017) 231-241.

[56] M.I. Mendelev, M.J. Kramer, R.T. Ott, D.J. Sordelet, D. Yagodin, P. Popel, Development of suitable interatomic potentials for simulation of liquid and amorphous Cu–Zr alloys, Philos. Mag., 89 (2009) 967-987.

[57] S. Nosé, A molecular dynamics method for simulations in the canonical ensemble, Mol. Phys., 52 (2006) 255-268.

[58] W.G. Hoover, Canonical dynamics: equilibrium phase-space distributions, Phys. Rev. A, 31 (1985) 1695.

[59] M. Parrinello, A. Rahman, Polymorphic transitions in single crystals: A new molecular dynamics method, J. Appl. Phys., 52 (1981) 7182-7190.

[60] Z. Pan, T.J. Rupert, Amorphous intergranular films as toughening structural features, Acta Mater., 89 (2015) 205-214.

[61] A.J. Cao, Y.Q. Cheng, E. Ma, Structural processes that initiate shear localization in metallic glass, Acta Mater., 57 (2009) 5146-5155.

[62] S.D. Feng, L. Qi, L.M. Wang, S.P. Pan, M.Z. Ma, X.Y. Zhang, G. Li, R.P. Liu, Atomic structure of shear bands in Cu64Zr36 metallic glasses studied by molecular dynamics simulations, Acta Mater., 95 (2015) 236-243.

[63] F. Shimizu, S. Ogata, J. Li, Theory of shear banding in metallic glasses and molecular dynamics calculations, Mater. Trans., 48 (2007) 2923-2927.

[64] Z.D. Sha, Q.X. Pei, V. Sorkin, P.S. Branicio, Y.W. Zhang, H.J. Gao, On the notch sensitivity of CuZr metallic glasses, Appl. Phys. Lett., 103 (2013) 081903.

[65] A. Stukowski, Visualization and analysis of atomistic simulation data with OVITO–the Open Visualization Tool, Modell. Simul. Mater. Sci. Eng., 18 (2010) 015012.

[66] D. Rodney, C. Schuh, Distribution of thermally activated plastic events in a flowing glass, Phys. Rev. Lett., 102 (2009) 235503.

[67] F. Shimizu, S. Ogata, J. Li, Yield point of metallic glass, Acta Mater., 54 (2006) 4293-4298.

[68] C. Gu, P. Huang, M.B. Liu, K.W. Xu, F. Wang, T.J. Lu, Intrinsic size effect of CuTa/Cu nanolaminates with unequal modulation ratios, Scripta Mater., 130 (2017) 100-104.

[69] S.P. Pan, S.D. Feng, J.W. Qiao, W.M. Wang, J.Y. Qin, Correlation between local structure and dynamic heterogeneity in a metallic glass-forming liquid, J. Alloys Compd., 664 (2016) 65-70.

[70] S.D. Feng, L. Qi, L.M. Wang, P.F. Yu, S.L. Zhang, M.Z. Ma, X.Y. Zhang, Q. Jing, K.L. Ngai, A.L. Greer, G. Li, R.P. Liu, Structural feature of $Cu_{64}Zr_{36}$ metallic glass on nanoscale: Densely-packed clusters with loosely-packed surroundings, Scripta Mater., 115 (2016) 57-61.

[71] J.W. Qiao, H.L. Jia, P.K. Liaw, Metallic glass matrix composites, Mater. Sci. Eng., R, 100 (2016) 1-69.

[72] Y.C. Kim, J.H. Na, J.M. Park, D.H. Kim, J.K. Lee, W.T. Kim, Role of nanometer-scale quasicrystals in improving the mechanical behavior of Ti-based bulk metallic glasses, Appl. Phys. Lett., 83 (2003) 3093-3095.

[73] H. Tsuzuki, P.S. Branicio, J.P. Rino, Structural characterization of deformed crystals by analysis of common atomic neighborhood, Comput. Phys. Commun., 177 (2007) 518-523.

[74] W. Guo, E.A. Jagle, P.P. Choi, J. Yao, A. Kostka, J.M. Schneider, D. Raabe, Shear-induced mixing governs codeformation of crystalline-amorphous nanolaminates, Phys. Rev. Lett., 113 (2014) 035501.

[75] B. Cheng, J.R. Trelewicz, Mechanistic coupling of dislocation and shear transformation zone plasticity in crystalline-amorphous nanolaminates, Acta Mater., 117 (2016) 293-305.

Figure Captions

Fig. 1 (a) Stress-strain curves of nanocomposites with different crystalline sizes: S1, S2, S3 and as cast. The insert shows the schematic of the S1 nanocomposite. Green represents crystallites, while gray represents MGs. (b) τ_y is to the global yield strength and τ_s is regarded as the flow strength. $\Delta\tau = \tau_y - \tau_s$ corresponds to a change in stress response.

Fig. 2 Atomic local shear strain of S1 nanocomposites at macroscopic strains of (a) 3%, (b) 5% and (c) 10%.

Fig. 3 (a) Potential energy, and only atoms with potential energy larger than -3 eV/atom are displayed. (b) Defects in the interfaces, characterized by QNA, and only atoms with the number of QNA (N_Q) larger than 5 atoms are shown at the initial configuration prior to deformation in the S2 nanocomposite. (c) Distribution of atomic Voronoi volume along the X coordinate (in the direction perpendicular to the loading direction).

Fig. 4 (a) The atomic displacement (yellow arrows) and local shear strain (atomic color) diagram of the portion of the S1 nanocomposite at the strain of 4%; (b) The common neighborhood parameter of the portion of the S1 nanocomposite at the strain of 4%, the interface is shown in a white rectangle.

Fig. 5 1/6<112> (Shockley) partial dislocation (green lines) and stacking fault (red atoms) of the S1 nanocomposite at strains of (a) 4%, (b) 5% and (c) 10%. For simplicity, all atoms belonging to the FCC structure are deleted.

Fig. 6 Atomic structure of the crystallites at strains of (a) 0% and (b) 10%. Green represents FCC, while red represents stacking faults formed via atomic shuffling. The red ovals denote dissolution processes of the FCC crystallites.

Fig. 7 At the strain of 10%, the local atomic shear strain of Cu/CuZr nanocomposites with different crystalline sizes: (a) S1; (b) S2; (c) S3 and (d) as cast.

Fig. 8 The proportions of atoms with η_{Mises} greater than the threshold value of 0.2 for the nanocomposites at different strains.

Fig. 9 At the strain of 4% (the yield point), the local atomic shear strain of Cu/CuZr

nanocomposites with different crystalline sizes: (a) S1; (b) S2; (c) S3 and (d) as cast.

Fig. 10 Potential energy, and only atoms with potential energy greater than -3 eV/atom are displayed at the initial configuration prior to deformation in the S1, S2 and S3 nanocomposites.

Fig. 11 Schematic representation of the interfaces in the role of coupled deformation processes. The interfaces are represented by the light blue, whereas the STZ distortions are depicted by the red. The stacking faults are represented by the pink, and dislocations are depicted by the green. The orange arrow indicates facilitating formation.

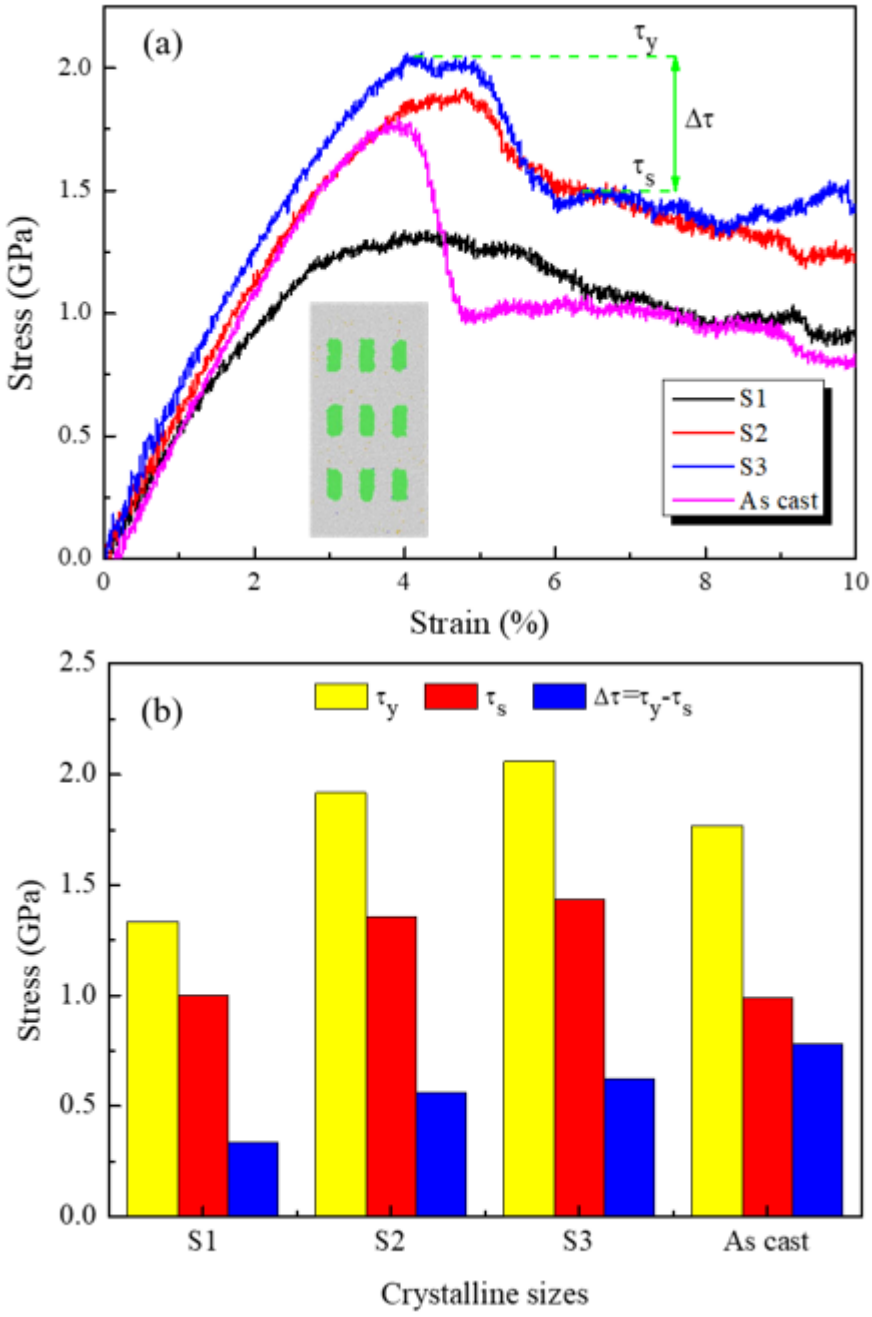

Fig. 1 (a) Stress-strain curves of nanocomposites with different crystalline sizes: S1, S2, S3 and as cast. The insert shows the schematic of the S1 nanocomposite. Green represents crystallites, while gray represents MGs. (b) τ_y is to the global yield strength and τ_s is regarded as the flow strength. $\Delta\tau = \tau_y - \tau_s$ corresponds to a change in stress response.

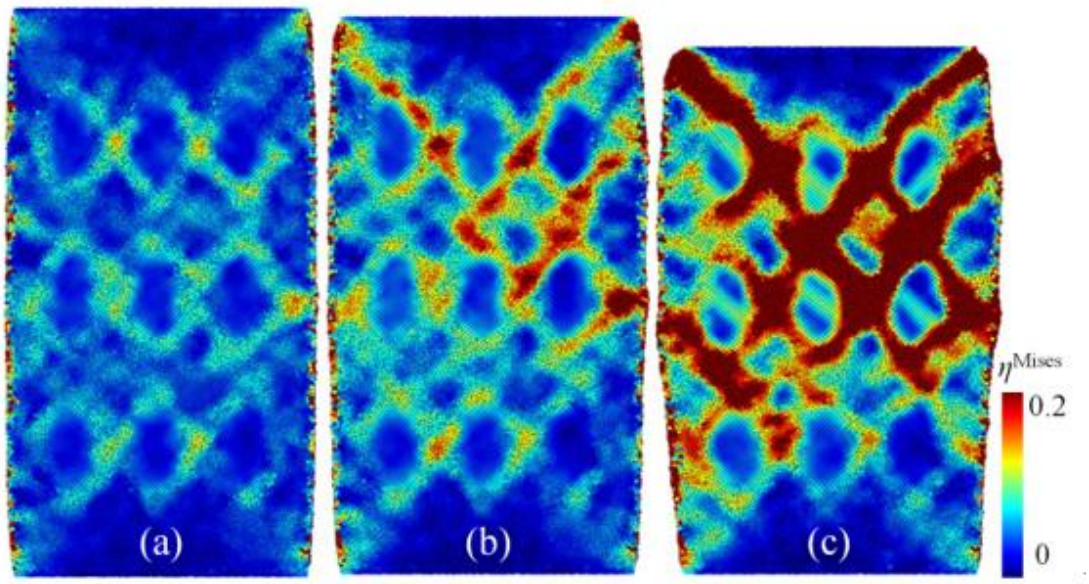

Fig. 2 Atomic local shear strain of S1 nanocomposites at macroscopic strains of (a) 3%, (b) 5% and (c) 10%.

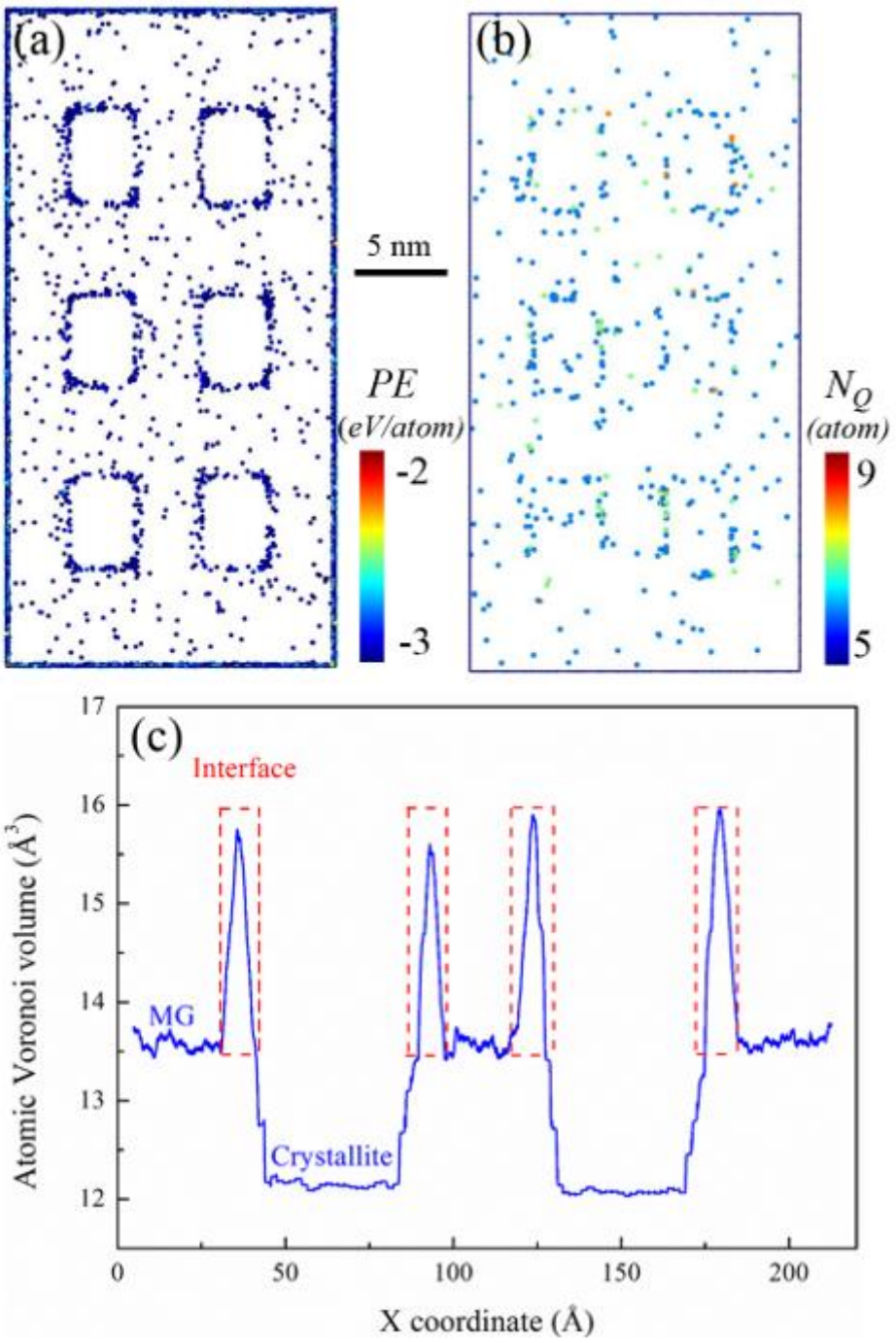

Fig. 3 (a) Potential energy, and only atoms with potential energy larger than -3 eV/atom are displayed. (b) Defects in the interfaces, characterized by QNA, and only atoms with the number of QNA (N_Q) larger than 5 atoms are shown at the initial configuration prior to deformation in the S2 nanocomposite. (c) Distribution of atomic Voronoi volume along the X coordinate (in the direction perpendicular to the loading direction).

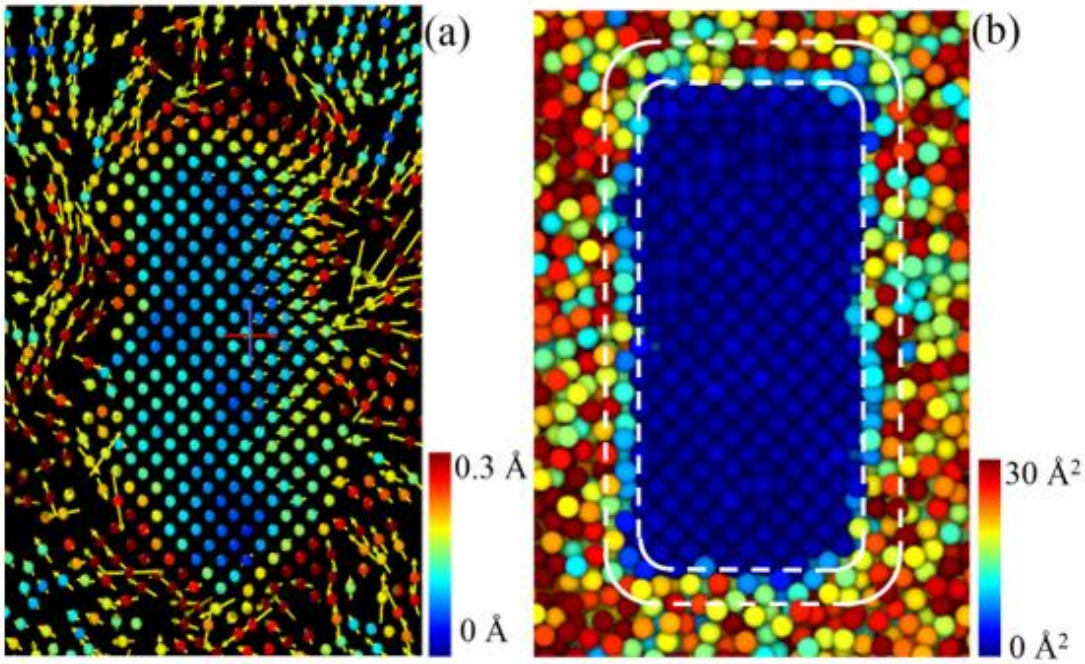

Fig. 4 (a) The atomic displacement (yellow arrows) and local shear strain (atomic color) diagram of the portion of the S1 nanocomposite at the strain of 4%; (b) The common neighborhood parameter of the portion of the S1 nanocomposite at the strain of 4%, the interface is shown in a white rectangle.

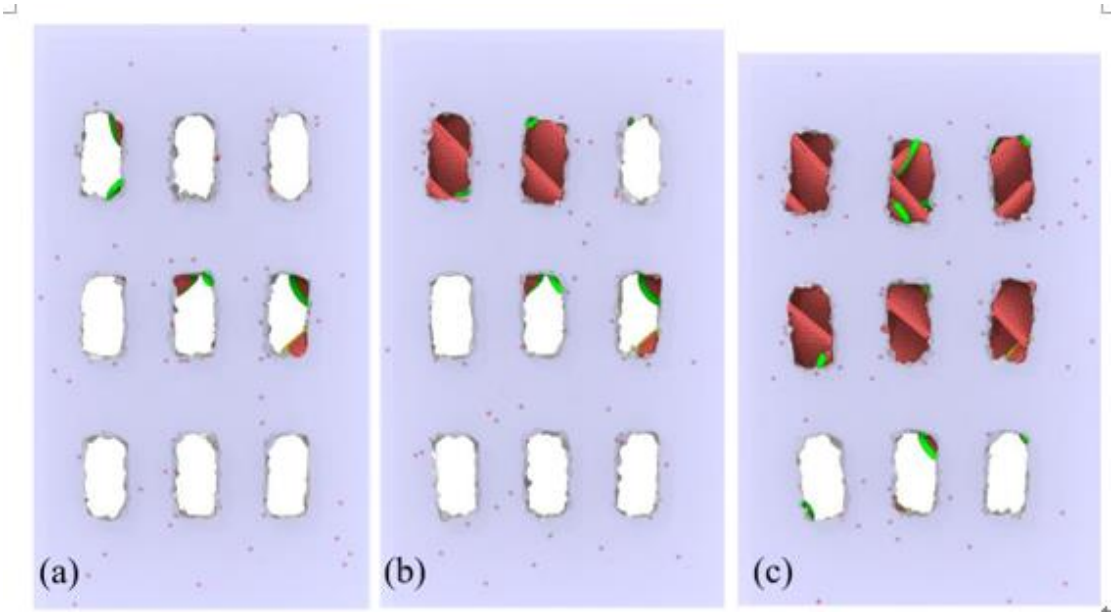

Fig. 5 1/6<112> (Shockley) partial dislocation (green lines) and stacking fault (red atoms) of the S1 nanocomposite at strains of (a) 4%, (b) 5% and (c) 10%. For simplicity, all atoms belonging to the FCC structure are deleted.

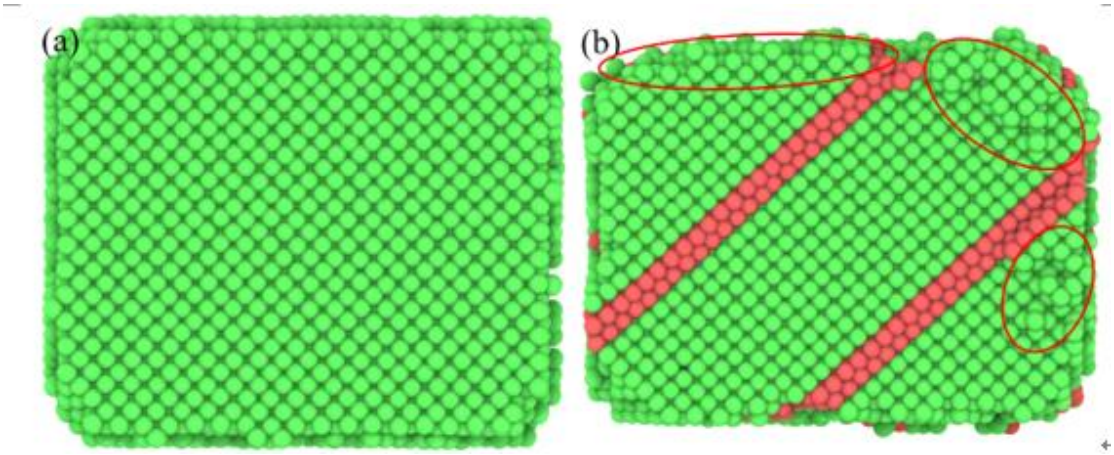

Fig. 6 Atomic structure of the crystallites at strains of (a) 0% and (b) 10%. Green represents FCC, while red represents stacking faults formed via atomic shuffling. The red ovals denote dissolution processes of the FCC crystallites.

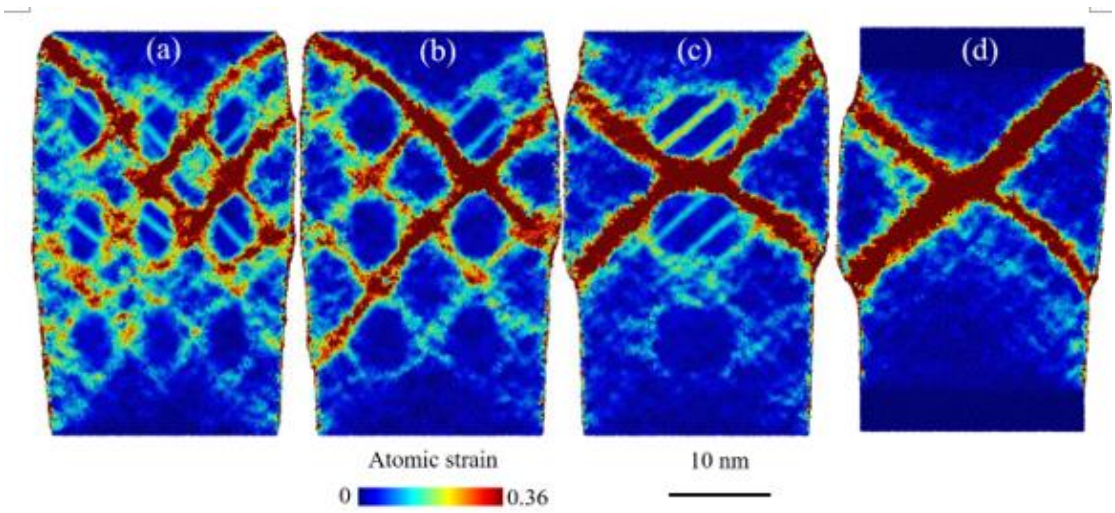

Fig. 7 At the strain of 10%, the local atomic shear strain of Cu/CuZr nanocomposites with different crystalline sizes: (a) S1; (b) S2; (c) S3 and (d) as cast.

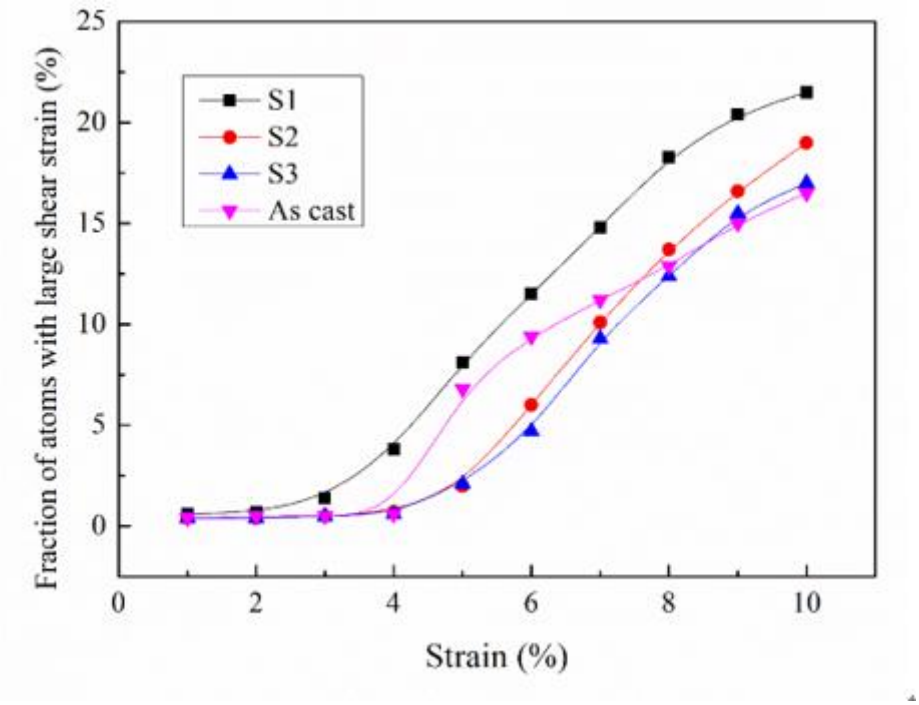

Fig. 8 The proportions of atoms with η_{Mises} greater than the threshold value of 0.2 for the nanocomposites at different strains.

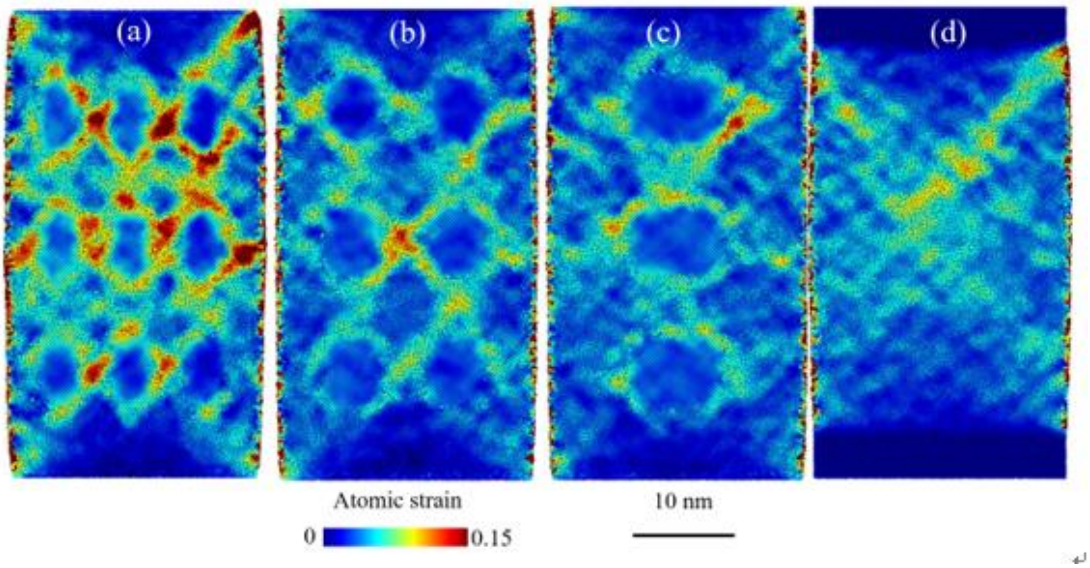

Fig. 9 At the strain of 4% (the yield point), the local atomic shear strain of Cu/CuZr nanocomposites with different crystalline sizes: (a) S1; (b) S2; (c) S3 and (d) as cast.

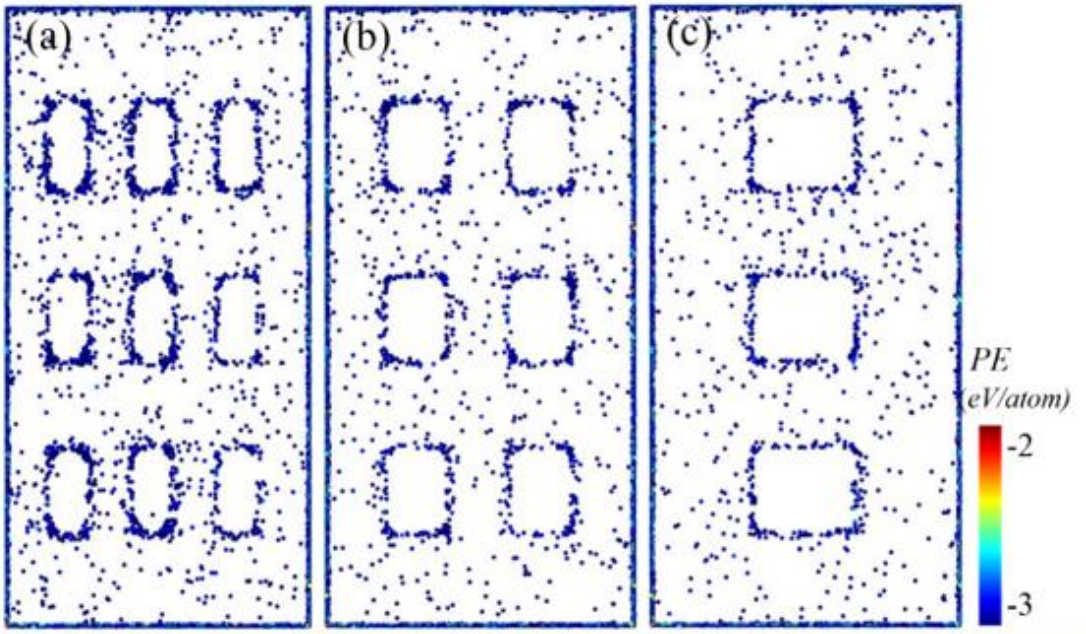

Fig. 10 Potential energy, and only atoms with potential energy greater than -3 eV/atom are displayed at the initial configuration prior to deformation in the S1, S2 and S3 nanocomposites.

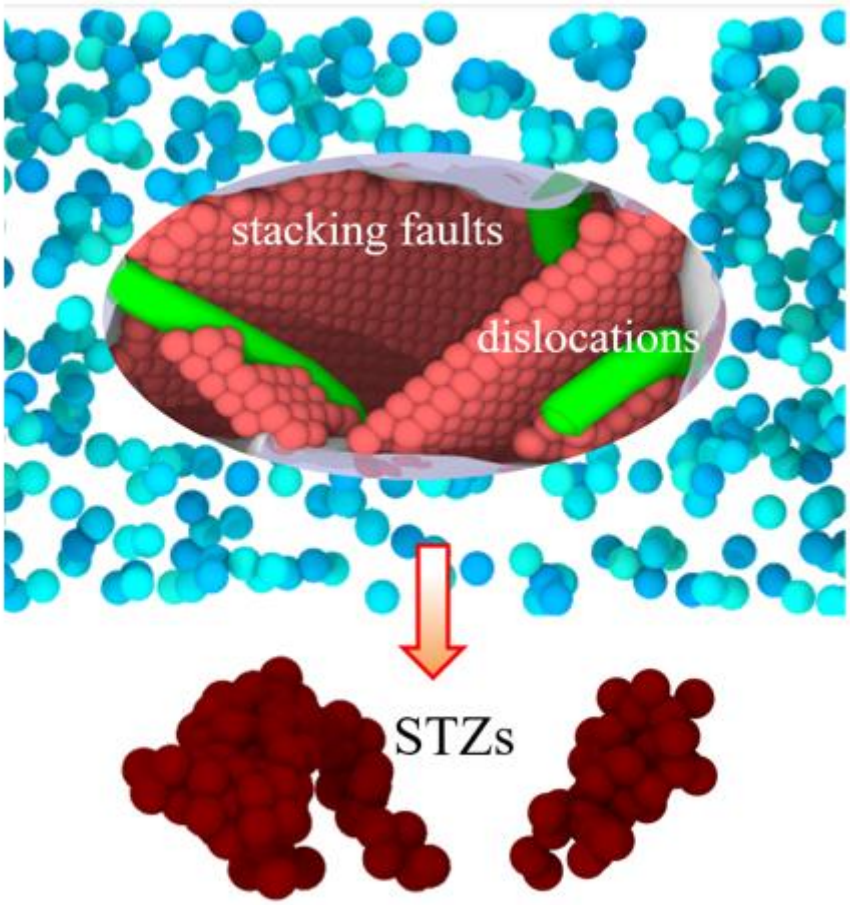

Fig. 11 Schematic representation of the interfaces in the role of coupled deformation processes. The interfaces are represented by the light blue, whereas the STZ distortions are depicted by the red. The stacking faults are represented by the pink, and dislocations are depicted by the green. The orange arrow indicates facilitating formation.